

Gravity Modes Reveal the Internal Rotation of a Post-mass Transfer Gamma Doradus/Delta Scuti Hybrid Pulsator in Kepler Eclipsing Binary KIC 9592855

Z. Guo^{1,2}, D. R. Gies², R. A. Matson²

1. *Copernicus Astronomical Center, Bartycza 18, 00-716 Warsaw, Poland;
guo@camk.edu.pl*

2. *Center for High Angular Resolution Astronomy and Department of Physics and Astronomy, Georgia State University, P. O. Box 5060, Atlanta, GA 30302-5060, USA;
gies@chara.gsu.edu, rmatson@chara.gsu.edu*

ABSTRACT

We report the discovery of a post-mass transfer Gamma Doradus/Delta Scuti hybrid pulsator in the eclipsing binary KIC 9592855. This binary has a circular orbit, an orbital period of 1.2 days, and contains two stars of almost identical masses ($M_1 = 1.72M_\odot$, $M_2 = 1.71M_\odot$). However, the cooler secondary star is more evolved ($R_2 = 1.96R_\odot$) while the hotter primary is still on the zero-age-main-sequence ($R_1 = 1.53R_\odot$). Coeval models from single star evolution cannot explain the observed masses and radii, and binary evolution with mass-transfer needs to be invoked. After subtracting the binary light curve, the Fourier spectrum shows low-order pressure-mode pulsations, and more dominantly, a cluster of low-frequency gravity modes at about 2 day^{-1} . These g-modes are nearly equally-spaced in period, and the period spacing pattern has a negative slope. We identify these g-modes as prograde dipole modes and find that they stem from the secondary star. The frequency range of unstable p-modes also agrees with that of the secondary. We derive the internal rotation rate of the convective core and the asymptotic period spacing from the observed g-modes. The resulting values suggest that the core and envelope rotate nearly uniformly, i.e., their rotation rates are both similar to the orbital frequency of this synchronized binary.

1. Introduction

Pulsating stars that show gravity modes are great assets to stellar astrophysics, because we can sound the deep interior through asteroseismology. Detailed analysis of their Fourier spectrum, especially for those on the main-sequence (Slowly Pulsating B stars and γ Doradus stars), only became available quite recently (Zwintz et al. 2017; Pápics et al. 2015, 2017; Van Reeth et al. 2015a), thanks to the continuous observations from space missions (e.g., *Kepler* : Borucki et al. 2010; *MOST* : Walker et al. 2003). Among these stars, the γ Dor pulsators, which are early-F to late-A type stars with $M \in [1.4M_{\odot}, 2.0M_{\odot}]$, are very common and have gained importance in the recent literature (Bedding et al. 2015; Van Reeth et al. 2015b, 2016; Schmid et al. 2016). Most of the well-studied γ Dor stars are single stars or they reside in very detached binaries, which can be treated as the result of single star evolution. Binary star evolution with mass transfer can also form δ Scuti and γ Dor variables (Chen et al. 2017), as well as other pulsating stars (subdwarf B stars: Vos et al. 2015; RR Lyraes and Cepheids: Karczmarek et al. 2017 and Gautschy & Saio 2017). Asteroseismology of these abnormal δ Scuti and γ Dor pulsators has not been carried out, and most of the past studies focused on the frequency analysis, e.g., oscillating Algol (oEA) systems (Mkrtichian 2002, 2003). In a previous paper (Guo et al. 2017), we have shown that the high-frequency p-modes observed in a post-mass transfer δ Scuti star in the eclipsing binary KIC 8262223 can be explained by the non-adiabatic calculations, albeit with some differences. In this work, we derive the accurate fundamental parameters of a post-mass transfer γ Dor/ δ Scuti hybrid in the eclipsing binary (EB) KIC 9592855 and decipher its g-mode pulsations. Those double-lined eclipsing binaries containing g-mode pulsators are ideal targets to refine our theory of stellar structure and evolution. For a list of 16 γ Dor pulsating EBs, please refer to Çakırlı et al. (2017).

KIC 9592855¹ ($\alpha_{2000}=19:35:04.833$, $\delta_{2000}=+46:14:11.70$, $K_p = 12.216$, $V = 12.255$) was first classified as a detached Algol-type eclipsing binary (AI*) in the All Sky Automated Survey (Pigulski et al. 2009). It was included in the *Kepler* Eclipsing Binary Catalog (Prša et al. 2011; Slawson et al. 2011). A set of light curve parameters is estimated from neural networks, including temperature ratio ($T_2/T_1 = 0.97$), sum of relative radius ($R_1/a + R_2/a = 0.489$), eccentricity and argument of periastron ($e \sin \omega = 0.0011$, $e \cos \omega = 0.0089$), and orbital inclination ($\sin i = 0.961$). The latest updates of the catalog are described in Kirk et al. (2016).

Debosscher (2011) did an automatic search for variabilities in the first Quarter light curves of *Kepler*, including KIC 9592855. The main frequencies they found are all orbital

¹2MASS J19350483+4614117, ASAS J193505+4614.2

harmonics: 1.6402 day^{-1} , 8.2010 day^{-1} , and 9.8412 day^{-1} , which are 2, 10, and 12 times of orbital frequency, respectively. Thus, these frequencies only indicate the binary nature, and the real pulsation frequencies are buried in the binary signal. Gies et al. (2012) measured the eclipse times of this binary, yielding an orbital period of $P = 1.21932475(2)$ days and the time of primary minimum of $T_0 = 2455656.3029(1)$ in Barycentric Julian Date (BJD), where 1σ uncertainties are given in parentheses in units of the last digits. Gies et al. updated their measurements using all 17 Quarters of *Kepler* data in Gies et al. (2015), and the updated ephemeris is $P = 1.21932487(2)$ and $T_0 = 2455691.664073(7)$. Conroy et al. (2014) also measured the eclipse timing variations of this system, together with 1278 short-period *Kepler* eclipsing binaries. The overall consensus is that there is no signature of a third companion to this binary, and the $O - C$ residuals scatter around zero with an amplitude of about 50 seconds. Throughout this work, we use the term ‘primary’ for the star that is in eclipse at the time of the deeper minimum (primary minimum) T_0 .

The latest photometry-derived atmospheric parameters reported by the *Kepler* team (Huber et al. 2014) are those based on Brown et al. (2011): $T_{\text{eff}} = 7513 \pm 262\text{K}$, $\log g = 3.946 \pm 0.4$, $[\text{Fe}/\text{H}] = -0.015 \pm 0.3$ and those updated in Pinsonneault et al. (2012): $(T_{\text{eff}}, \log g, [\text{Fe}/\text{H}]) = (7498, 3.964, -0.060)$. A mass of $1.73M_{\odot}$ is derived from fitting the Dartmouth isochrones (Dotter et al. 2008) in the $\log g - T_{\text{eff}}$ plane. The binary spectral energy distribution (SED) fitting of Armstrong et al. (2014) yields effective temperatures of the primary and secondary star as $7934 \pm 381\text{K}$ and $7805 \pm 570\text{K}$, respectively.

This article is organized as follows. In Section 2, we describe how the photometric and spectroscopic data are analyzed. It includes characterizing the atmospheric properties of individual components and detailed binary modeling. Section 3 details the interpretation of the pulsation spectrum, a general comparison between observations and the theoretically unstable modes, the identification of a series of prograde dipole g-modes and how the internal rotation is derived, and in the end the evolutionary history of this binary. In the final section (Sec. 4), we summarize our results and discuss prospects for future work.

2. Observations and Binary Modeling

2.1. Spectral Characteristics of Individual Components

As one of the systems from our sample of 41 *Kepler* eclipsing binaries in a *Kepler* GO program (Gies et al. 2012), KIC 9592855 was observed with the RC Spectrograph mounted on the 4 meter Mayall telescope at the Kitt Peak National Observatory (KPNO). We obtained seven spectra with moderate resolving power ($R = \lambda/\delta\lambda \approx 6000$) in the wavelength range of

3930 – 4610 Å.

We show one of the observed double-lined spectra in Figure 1 (green line). At the orbital phase of 0.18, the two components are clearly separated in the cores of the Balmer lines ($H\delta\lambda 4102$ and $H\gamma\lambda 4341$). We measured the Doppler shifts of the spectral lines by cross-correlating the observed spectra with templates from the UVBLUE library (Rodríguez-Merino et al. 2005). The detailed data reduction and cross-correlation procedures can be found in Matson et al. (2016). The derived radial velocities for this target together with the other 40 *Kepler* eclipsing binaries listed in Gies et al. (2012, 2015) will be presented in a separate paper (Matson et al. 2017, in prep.).

We implemented the Doppler tomography algorithm (Bagnuolo & Gies 1991) to get the individual spectrum of each component. In this algorithm, the linear inverse problem of spectral separation was solved with an iterative method in the wavelength domain. Other methods include those based on Singular Value Decomposition (Hadrava 1995; Ilijic 2004) and MCMC (Czekala et al. 2017). We determined the mean flux ratio of the two stars in the observed spectral range (≈ 4225 Å) as $F_2/F_1 = 0.98 \pm 0.04$. The separated individual spectrum was compared with a grid of synthetic spectra from the UVBLUE library to determine the atmospheric parameters: T_{eff} , $\log g$, $v \sin i$, and $[\text{Fe}/\text{H}]$ following the method detailed in Guo et al. (2016). In brief, the method includes fixing the value of surface gravity $\log g$ to those from the ELC binary modeling and optimizing the remaining parameters in a chi-square-minimization sense with both the genetic algorithm *PIKAIA* (Charbonneau 1995) and the gradient-based Levenberg-Marquardt algorithm². The 1σ uncertainties were determined by varying the parameters so that χ^2 increased by 1.0 from the minimum value in the former algorithm, and from the local covariance matrix in the latter algorithm. The results of the two methods agree very well and are summarized in Table 1.

In Figure 1, we display the reconstructed individual spectrum of each star (black) and their best-fitting models (red). The spectra of the two components have similar overall appearances, although the derived effective temperature of the secondary star is higher ($T_{\text{eff}1} = 7092 \pm 50\text{K}$, $T_{\text{eff}2} = 7565 \pm 57\text{K}$). However, the ratio of the eclipse depth in the *Kepler* light curve indicates that the secondary star is slightly cooler than the primary. We discuss this discrepancy in the following section 2.2. The secondary also has a slightly faster projected rotational velocity ($(v \sin i)_1 = 64 \pm 9 \text{ km s}^{-1}$, $(v \sin i)_2 = 70 \pm 10 \text{ km s}^{-1}$). Both components have essentially a solar metallicity within $\sim 1\sigma$ ($[\text{Fe}/\text{H}]_1 = -0.06 \pm 0.05$ and $[\text{Fe}/\text{H}]_2 = 0.04 \pm 0.05$).

²The MPFIT package by Craig B. Markwardt

2.2. *Kepler* Photometry and Binary Modeling

Broadband photometric data of KIC 9592855 with micro-magnitude precision were collected by the *Kepler* satellite from Q1 to Q17. We use the available long cadence Simple Aperture Photometry (SAP) light curves with a sampling rate of 29.44 minutes. The light curves were obtained from the Mikulski Archive for Space Telescopes (MAST) and prepared following several procedures (5σ clipping of outliers, removing of low-frequency trend with splines, and median value corrections, etc.) detailed in Guo et al. (2016). We adopted a mean contamination factor³ of $k = 0.004$ over all quarters.

The light curve synthesis code ELC (Orosz & Hauschildt 2000), originally designed to model X-ray binaries, can also be used to model detached/semi-detached eclipsing binaries, non-eclipsing binaries, and transit light curves of exoplanets. It is used to model the binary light curves (LCs) and radial velocities (RVs) of KIC 9592855 simultaneously. The synthetic LCs and RVs are calculated from integrating the specific intensities from the NextGen model atmosphere (Hauschildt et al. 1999) over the stellar surface described by the Roche model. We assume a circular orbit with synchronized rotations as suggested by spectroscopy. Due to the sharp differences between the quality and quantity of LCs and RVs (micro-magnitude vs. km s^{-1} precision, ~ 50000 LC data points vs. 7 RV measurements), we have to scale the errors of RVs so that RVs and LCs have comparable contributions to the total chi-squares. The genetic algorithm PIKAIA is implemented to find the best combination of parameters. The fitting parameters include those that impact the light curves ($i, f_1, f_2, T_{\text{eff}2}, l_1, l_2$) and those that mainly affect the radial velocities (K_1, q, γ). The effective temperature of the primary star is fixed to the spectroscopic value ($T_{\text{eff}1} \equiv 7100$ K). The orbital eccentricity (e) is fixed to zero, and the gravity darkening coefficients (β) are fixed to the canonical value 0.08 associated with the stellar envelope properties (convective). The detailed definitions of all the parameters can be found in Table 2. The orbital period (P) and the time of primary minimum (T_0) are fixed to values derived by Gies et al. (2015). These ephemeris parameters are of high precision, and experiments show that letting them vary does not improve the light curve fit.

Our initial binary solution from ELC suggests that the secondary has a slightly lower temperature ($T_{\text{eff}2}/T_{\text{eff}1} = 0.987$, $T_{\text{eff}1} \equiv 7100$ K, $T_{\text{eff}2} = 7003$ K). However, the spectroscopic value of $T_{\text{eff}2}$ in Table 1 is ~ 500 K higher ($T_{\text{eff}2} = 7565$ K). This small discrepancy also exists in other studies, e.g., the secondary star in KIC 3858884 has $T_{\text{eff}2} = 6890$ K from the spectroscopic analysis which is ~ 300 K higher than that from the light curve (Maceroni et al.

³ ELC corrects the effect of aperture contamination of flux from nearby stars by adding to the median value of the model light curve y_{med} an offset $ky_{\text{med}}/(1 - k)$.

2014). We found that we can get almost the same temperature ratio $T_{\text{eff2}}/T_{\text{eff1}} = 0.987 \pm 0.010$ with different fixed values of T_{eff1} (7100, 7200, 7300, 7400 K). Thus the temperature ratio is well determined from the light curve, but the individual temperatures are only approximately determined. It also suggests that the uncertainties of the spectroscopic temperatures in Table 1 are probably underestimated. The way to break the temperature degeneracy and to reconcile the above discrepancy is to adopt the temperature solutions that are both close to the mean value of spectroscopic temperatures $T_{\text{eff}}(\text{mean}) = 7328$ K since the temperature ratio is very close to one. The final adopted effective temperatures are $T_{\text{eff1}} \equiv 7300$ K and $T_{\text{eff2}} = 7202$ K. Note that different fixed values of T_{eff1} do not have a significant effect on other binary parameters. Our final binary model is shown in Figure 2, and the associated ELC parameters are listed in Table 2. Our binary model can fit the LCs and RVs very well. The model suggests the primary and secondary star have almost identical masses ($M_1 = 1.72M_\odot$, $M_2 = 1.71M_\odot$) but very different radii ($R_1 = 1.53R_\odot$, $R_2 = 1.96R_\odot$). The implications of these measurements on the evolutionary history are presented in Section 3.4. The $v \sin i$ values from our synchronized binary model agree with the spectroscopic ones within 1σ .

The light curve residuals still show sinusoidal variations with an amplitude of ~ 0.002 mag, and they arise from an imperfect match of ellipsoidal variations. The sinusoidal shape over the whole four-year dataset implies that they are not due to spots or stellar activities. We tried to change the reflection parameter, gravitational darkening coefficient, and even the rotation period, but this mismatch persists. We conclude that it is possibly due to the limitations of the ELC model or the optimization algorithm. Indeed, the high-precision of *Kepler* light curves have called for the need for a refinement of our binary modeling tools (e.g., Prša et al. 2013).

3. Asteroseismology and Binary Evolution

3.1. Pulsational Properties

We subtracted the best-fitting binary light curve from the original data and did a Fourier analysis of the pulsation residuals. There are still some systematic residuals in the eclipses (Figure 2). These residuals appear sinusoidal and they generate some aliases of orbital harmonics of low amplitudes in the Fourier spectrum. To remedy this, we generate a simple binary light curve model by binning the phase-folded light curve. This model can fit the data equally well, but the pulsation residuals have much better quality in the eclipses. We thus proceed in our analysis using these residuals.

The Fourier spectrum was calculated to the Nyquist frequency of *Kepler* long cadence data ($f_{\text{Nyquist}} = 24.46 \text{ d}^{-1}$). The significant frequencies (using the classical criterion of the signal to noise ratio $S/N > 4$) were extracted with the pre-whitening procedures implemented with the *Period 04* package (Lenz & Breger 2005). These extracted frequencies are enumerated in the order of decreasing S/N , and they are listed in Table 3 and 4. The uncertainties are calculated following the treatment in Kallinger et al. (2008). In Figure 3, we show a section of the pulsation residuals and the corresponding Fourier amplitude spectrum.

In the pulsation spectrum, the dominant pulsational frequencies cluster around $\sim 2 \text{ day}^{-1}$, and the strongest pulsation mode is at 2.2326 day^{-1} . Close inspection reveals that these low-frequency pulsations belong to a series of prograde dipole g-modes. The detailed analysis will be presented in Section 3.3, and the parameters of these pulsation modes are listed in Table 3.

There are also several strong peaks at around 10, 14, 21, and 24 day^{-1} ($f_7 = 9.9353$, $f_8 = 13.8850$, $f_{21} = 21.3112$, $f_{24} = 24.4334 \text{ day}^{-1}$, respectively). Many low-amplitude peaks are present across the whole spectrum. Since there are significant frequencies close to f_{Nyquist} , we also check the super-Nyquist spectrum (Figure 3). All the frequencies above f_{Nyquist} have lower amplitudes than their mirror-reflected counterparts. Thus the peaks contained in $< f_{\text{Nyquist}}$ range are indeed real pulsations.

We identified the combination frequencies in the form of $f_k = m f_i \pm n f_j$ or $f_i \pm m f_{\text{orb}}$, where m, n are integers satisfying $1 \leq (m, n) \leq 2$ (Table 4). The majority of the combination frequencies are in the latter form, and they are due to the amplitude modulation by eclipses.

The overall appearance of the spectrum agrees with that of an evolved δ Scuti star of $T_{\text{eff}} \sim 7000 \text{ K}$ (e.g., KIC 9851944 in Guo et al. 2016). We next discuss the nature of these pulsations and examine whether the observed frequencies agree with the unstable range of pulsation modes (Section 3.2).

3.2. A General Overview of Unstable Modes

The upper panel of Figure 4 shows the evolution of theoretical frequencies of $l = 0, 1, 2$ modes (black circles, red triangles, and green squares, respectively) associated with a non-rotating interior model of $1.70 M_{\odot}$. The calculation was performed from Zero Age Main Sequence (ZAMS) ($R = 1.5 R_{\odot}$) to Terminal Age Main Sequence (TAMS) ($R = 2.3 R_{\odot}$). The interior models and the oscillation frequencies are calculated with MESA (v8118) (Paxton et al. 2011, 2013, 2015) and GYRE (v4.3) (Townsend & Teitler 2013), respectively. We adopt the solar mixtures of Grevesse & Sauval (1998), with the metal mass fraction $Z = 0.02$ and

an initial Helium abundance of $Y = 0.28$. The OPAL opacity table (Iglesias & Rogers 1996) is used, and convective overshooting is neglected. The mixing length parameter is fixed to the solar-calibrated value of $\alpha_{\text{MLT}} = 1.8$. The set-up above is consistent with observations of KIC 9592855 since we derive a solar metallicity and a mass of about $1.7M_{\odot}$ for both components. The filled symbols indicate unstable modes.

The stability parameter, η , which is the normalized growth-rate defined in Stellingwerf (1978) (the integration of differential work $\frac{dW}{dr}$ over the whole star, $\eta = \int_0^R (\frac{dW}{dr})dr / \int_0^R |\frac{dW}{dr}|dr$) can be used as a proxy for the intrinsic mode amplitude. Positive values of η indicate modes are excited. We find that the η values from GYRE’s non-adiabatic calculation are not numerically well-behaved for modes of very low-frequencies, and the variation of η as a function of frequency is not continuous and smooth. This problem is especially severe for high-order g-modes. Thus we re-calculate the pulsation modes with Dziembowski’s non-adiabatic code (Dziembowski 1971,1977) NADROT. The theoretical frequencies from the two codes show excellent agreement, but the η values from NADROT are more robust.

We choose the best-matching interior model for the secondary star with $M_2 = 1.7M_{\odot}$, $R_2 = 1.96R_{\odot}$ from the above evolutionary sequence. The associated pulsation frequencies and the variations of η are shown in the lower panel of Figure 4. For convenience, we also over-plot the observed Fourier spectrum and scale it to have a maximum amplitude of 0.4. We can roughly divide the variations of the instability parameter η into two regimes. For p-modes, with frequencies $f \geq 14 \text{ day}^{-1}$, the variation of η is independent of spherical degree l . Several low order p-modes (p_1, p_2, p_3, p_4) are excited. Note that the p_5 radial mode from NADROT is unstable, but it only has a very small positive η . In GYRE, it is barely damped. This is due to the delicate balancing between damping and driving for such a mode. In the g-mode regime ($f < 14 \text{ day}^{-1}$), the stability parameters η are l -dependent, and this is especially true for high-order modes. Only the lowest-order g-modes are unstable ($n = -1, -2$), and all higher-order modes ($< 10 \text{ day}^{-1}$) have negative η , i.e., they are damped.

The theoretically unstable modes are low-order p- and g-modes, from $\sim 10 \text{ day}^{-1}$ to $\sim 30 \text{ day}^{-1}$. They can explain the observed frequency peaks from $\sim 10 \text{ day}^{-1}$ to $\sim 24 \text{ day}^{-1}$. The low-frequency modes observed ($f < 10 \text{ day}^{-1}$), especially the cluster of high-amplitude modes around 2 day^{-1} , cannot be explained by our calculations. However, there is a local peak in η values near 2 day^{-1} , indicating that these modes could be excited if some kind of driving mechanism is added. It is not surprising that our non-adiabatic calculation based on the frozen-convection approximation cannot excite low-frequency g-modes. This is actually the major problem in our theory for the mode excitation mechanism: the theory can well explain the excitation of pulsations in β Cephei stars, Slowly Pulsating B-stars (SPB), and hot δ Scuti stars (e.g. Pamyatnykh 1999), but it cannot excite the low-frequency g-modes

observed in cool δ Scuti stars as well as γ Dor stars. Guzik et al. (2000) attributed the driving of γ Dor stars to the ‘convective blocking mechanism’, and a robust theory of time-dependent pulsation-convection interaction is still desirable, e.g., Dupret et al. (2005) and Xiong et al. (1997, 2015, 2016).

The above discussion suggests that the observed pulsations are consistent with the properties of the secondary star. Is the primary star pulsating? This is a common problem in the analysis of pulsating binaries, i.e., the determination of the pulsation origin. This issue can be resolved by examining the light travel time effect (phase modulation or amplitude modulation, Shibahashi & Kurtz 2012; Murphy et al. 2014; Schmid et al. 2015). Regrettably, this method does not work for KIC 9592855 with such a short orbital period ($P = 1.2$ d). The eclipse mapping method (Reed 2005; Bíró & Nuspl 2011), i.e., by inspecting the pulsation amplitude/phase variations in eclipses, can in principle determine the origin of pulsations and even identify the pulsation modes. But it is technically challenging and still awaits its application to a real star. With a mass and radius of $M_1 = 1.72M_\odot$ and $R_1 = 1.53R_\odot$, the primary star is essentially on the ZAMS, and if it were pulsating, the unstable range of p-modes should be at about $35 - 40 \text{ day}^{-1}$ (p_3, p_4). This range is somewhat higher than the frequencies observed ($0 - 25 \text{ day}^{-1}$). Thus from the perspective of the theoretically unstable frequency range, the observed pulsations of KIC 9592855 agree with the theoretical predictions for the secondary star, but we cannot completely rule out the possibility that the primary is pulsating.

One caveat: as will be detailed in Section 4, this system may have gone through the binary evolution with mass transfer. The above analysis is based on the assumption that an interior structure model from single star evolution with the observed mass and radius can be used to infer the pulsational spectrum. It has been shown that this assumption is probably valid, as the p-mode pulsations of a post-mass transfer, rejuvenated δ Scuti star in KIC 8262223 (Guo et al. 2017) can indeed be explained by using a model from single star evolution. The delicate effects of mass-transfer on the pulsations need further investigation. We also leave the detailed asteroseismic modeling of the observed individual frequencies to a future study and concentrate on the equally-spaced g-mode pattern in Section 3.3.

3.3. Identification of Prograde Dipole g-modes Affected by Rotation

In the g-mode regime, the dominant frequency peaks are around 2 day^{-1} (Figure 3). These peaks are almost equally spaced in period. In Figure 5, we have marked these peaks with red dotted lines. In the order of increasing period, they are $f_{24} = 30.538, f_9 =$

32.3392, $f_*^4 = 34.0459$, $f_3 = 35.6630$, $f_6 = 37.2075$, $f_1 = 38.6991$, $f_{18} = 40.1458$ in units of 1000 seconds. Table 3 contains the details of these pulsations. A careful examination reveals that the period spacings decrease monotonically, from $dP = 1.8$ at period of ~ 3200 s to $dP = 1.6$ at period ~ 4000 s. In the period-spacing vs. period diagram ($dP - P$) shown in Figure 7, this decline of period spacings manifests itself as a downward (negative) slope. This is clearly the signature of rotational effects on high-order g-modes. A linear fit to the observed $dP - P$ yields a slope of $\Sigma = -0.043$. This slope directly relates to the internal rotation of the star as will be elaborated below.

With the goal of modeling the slope of the period spacing pattern, and largely following Van Reeth et al. (2016), we begin with the asymptotic relation for high-order g-modes (Tassoul 1980) without rotation. The pulsation period is given by:

$$P_{nl} \approx \frac{\Pi_0}{\sqrt{l(l+1)}}(n+0.5), \quad (1)$$

where n is the radial order, l is the spherical degree, $\Pi_0 = 2\pi^2(\int_{r_1}^{r_2} \frac{N}{r} dr)^{-1}$, and N is the Brunt-Väisälä frequency. The integration in the expression of Π_0 is performed within the g-mode propagation cavity $r_1 \rightarrow r_2$. The asymptotic period spacing is:

$$\Delta\Pi_l = \frac{\Pi_0}{\sqrt{l(l+1)}}. \quad (2)$$

The observed period spacing is usually indicated by dP , but the theoretical asymptotic period spacing is denoted by $\Delta\Pi_l$. The period spacing $\Delta\Pi_l$ is a constant for fixed spherical degree l and for a fixed stellar interior model. For γ Dor stars, which generally have a convective core, $\Delta\Pi_l$ decreases monotonically from ZAMS to TAMS. This is mainly because the g-mode cavity becomes deeper and larger as a result of the retreat of the convective core, making the integration $\int \frac{N}{r} dr$ larger and thus Π_0 smaller (e.g., Fig.10 in Schmid et al. 2016).

With rotation, the period spacing pattern in the observer’s (inertial) frame contains a linear trend, and the slope of this trend is either negative for zonal ($m = 0$) and prograde⁵ ($m > 0$) modes or mainly positive for retrograde modes ($m < 0$). The observed slope results from the transformation of pulsation frequencies from the co-rotating frame (*co*) to the inertial frame (*in*): $f_{in} = f_{co} + m f_{rot}$, and also from the reduction or increase of pulsation

⁴This frequency peak has a signal-to-noise ratio slightly lower than 4 ($S/N \sim 3.6$) with our adopted noise level. Since it complies with the period spacing pattern, it is very likely to be a real pulsation. We thus include it but use a different notation f_* .

⁵We assume the mode eigenfunctions have the time dependence of $\propto e^{-i\omega t}$.

periods due to rotation. The latter can be characterized by the relation which invokes the traditional approximation:

$$P_{co} \approx \frac{\Pi_0}{\sqrt{l_{\text{eff}}(l_{\text{eff}} + 1)}}(n + 0.5), \quad (3)$$

where $l_{\text{eff}} = (\sqrt{1 + 4\lambda_{l,m,s}} - 1)/2$ is the effective spherical degree introduced by Townsend (2005). With the introduction of l_{eff} , the asymptotic relation for period is in the same form of the non-rotating case of eq. (1). $s = 2f_{\text{rot}}/f_{co}$ is the spin parameter, and $\lambda_{l,m,s}$ are the eigenvalues of the Laplace tidal equations, which are the reciprocal of the eigenvalues of matrix \mathbf{W}^{-1} defined in, e.g., Unno et al. (1989) (eq. 34.29, 34.30). In the zero-rotation limit ($s \rightarrow 0$), $\lambda_{l,m,s} \rightarrow l(l+1)$ and $l_{\text{eff}} \rightarrow l$. For prograde and zonal g-modes, $\lambda_{l,m,s}$ increases with s except for prograde sectoral modes ($l = m$). To facilitate the inspection of equation (3), we show the variations of $\lambda_{l,m,s}$ for zonal and prograde modes of $l = 1 - 4$ in Figure 6. They are calculated with the *astro_hough* subroutine in GYRE.

To model the observed $dP - P$, we generate synthetic g-modes with a grid of consecutive radial orders n in the co-rotating frame (eq. 3) and transform them to the inertial frame. This grid of periods can then be interpolated to the observed values of pulsation periods, and a χ^2 -minimization can be performed with P and dP as independent and dependent variables, respectively. This modeling procedure only involves two free parameters: the rotation frequency f_{rot} and the asymptotic period spacing $\Delta\Pi_l$ (or $\Delta\Pi_0$). It is also assumed that l and m are known. In practice, although multiple combinations of l and m may fit the observed $dP - P$ equally well, we can usually determine the correct (l, m) combination by comparing the resulting $\Delta\Pi_l$ to the expected theoretical values. This method does not need the time-consuming calculation of evolutionary interior models and thus can be applied to a large sample of stars. For example, Van Reeth et al. (2016) did an ensemble analysis of internal rotations by using the period spacing pattern for a sample of 68 γ Dor stars.

Ouazzani et al. (2017) did extensive calculations of pulsation periods by using both the traditional approximation and their 2-D code. Their results can give some guidance on modeling KIC 9592855. First, there is a near one-to-one relation between the slope Σ and rotation frequency f_{rot} , and this relation is relatively insensitive to metallicity and additional mixing near the edge of the convective core (convective overshooting, microscopic diffusion, etc.). Second, only zonal and prograde modes have a downward slope, i.e., negative Σ . The slope of zonal modes never exceeds -0.025 ; thus the observed $\Sigma = -0.043$ in KIC 9592855 indicates prograde modes.

From the perspective of geometric cancellation over the stellar disk, usually only $l = 1$ and $l = 2$ g-modes can be observed in the broad-band photometric data of *Kepler*.

KIC 9592855 also has a high inclination ($i = 73^\circ.3$), assuming pulsation-spin-orbit alignment, which indicates that $(l = 1, m = 1)$ modes have a higher visibility than $(l = 1, m = 0)$ modes (Gizon & Solanki 2003). Similarly, $(l = 2, m = 2)$ modes are more visible than $(l = 2, m = 0)$ and $(l = 2, m = 1)$ modes.

Thus assuming $l = 1, m = 1$, we fit the observed $dP - P$ by using the procedure mentioned above. This results in $f_{\text{rot}} = 0.8 \pm 0.1 \text{ day}^{-1}$ and $\Delta\Pi_{l=1} = 3.0 \pm 0.2$ (in 1000 sec). The best-fitting model and the contour plot of χ^2 values are shown in the right two panels of Figure 7. The left panel shows the period échelle diagram, with periods modulo a fixed spacing of 1600 seconds. The g-modes belonging to the consecutive prograde dipole modes form a parabolic ridge, indicating period spacings that decrease linearly with periods. This is the signature of fast rotation in the échelle diagram. For more such examples, please refer to Bedding et al. (2015).

We find that $(l = 2, m = 2)$ modes can also fit the $dP - P$ pattern with similar chi-square values, but the resulting asymptotic period spacing is $\Delta\Pi_{l=2} = 3200$ seconds, which is too large to be associated with $l = 2$. We can thus safely discard this possibility. This is the same method used in Van Reeth et al. (2016) for mode differentiation. The identification of $l = 1, m = 1$ g-modes in KIC 9592855 also agrees with their discovery that the prograde dipole modes prevail in the γ Dor stars.

Note that the method discussed above is only approximate. By comparing with theoretical frequencies from evolutionary models, detailed modeling of individual g-mode frequencies can refine the rotation rates and asymptotic period spacings. The f_{rot} measured from the period spacing slope of g-modes is an averaged value over the Brunt-Väisälä frequency N . It can thus be treated as the rotation rate of the convective core boundary, since this transition region with its chemical composition gradient has the largest contribution to N and thus to the period spacing (Miglio et al. 2008). It is expected that within the chemically homogeneous radiative envelope the rotation rate should be nearly uniform (Pamyatnykh et al. 2004). A large rotational gradient may occur mainly in the transition zone around the convective core.

It is interesting to note that the derived interior rotation rate $f_{\text{rot}} = 0.8 \pm 0.1 \text{ day}^{-1}$ is very close to the surface rotation frequency, which is the same as the orbital frequency $f_{\text{orb}} = 0.8201 \text{ day}^{-1}$. Thus the envelope and the core rotate almost uniformly. This is the first measurement of the interior rotation of F- or A-type stars in a synchronized close binary system. The two F-star components in the eccentric binary system KIC 10080943 (Schmid et al. 2015) also show near-uniform interior rotation, as revealed from the splitting of g-modes.

For single stars, near uniform rotation has been measured in a few F- or A-type stars

(KIC 9244992 in Saio et al. 2015; KIC 1145123 in Kurtz et al. 2015; KIC 7661054 in Murphy et al. 2016) as well as a B-type star HD 157056 (Briquet et al. 2007). These measurements are mostly from rotational splittings of envelope-sensitive p-modes and core-sensitive g-modes, which limit the application to slow rotators. Several case studies of B-type stars reveal faster rotating cores (HD 129929 in Dupret et al. 2004; ν Eridani in Pamyatnykh et al. 2004). On the contrary, Triana et al. (2015) discovered that the SPB star KIC 10526294 has a much faster-rotating envelope than its core (\sim three times) and in the opposite direction. Recently, Pápics et al. (2017) reported a sample of SPB stars with period spacing patterns affected by rotation. However, the $dP - P$ patterns are not fully exploited to derive core-to-envelope differential rotation. Ouazzani et al. (2017) derived the internal rotation rates for four γ Dor stars (KIC 4253413, KIC 6762992, KIC 5476299, and KIC 4177905), but no information on the envelope rotation is provided.

All these intermediate and massive stars possess a convective core and radiative envelope. The numerical simulations by Rogers et al. (2013, 2015) prove that the transport of angular momentum by internal gravity waves (IGW) can explain all the aforementioned rotation profiles in single stars. The angular momentum transport in early-type binary stars involves the consideration of tidally excited gravity waves instead of the convection-driven IGW in the single-star case. These tidally driven oscillations are excited near the convective-radiative interface and propagate inside the radiative envelope and dissipate due to radiative diffusion and non-linearity near the surface (Goldreich & Nicholson 1989). They are the primary source for the orbit and spin decay and have been used to explain successfully the circularization and synchronization of early-type binaries (Zahn 1975, 2008)

Goldreich & Nicholson (1989) suggest that the stellar surface may be synchronized first, and thus the stars spin down or up from outside inward. In line with this argument, Kallinger et al. (2017) found that the surface layer of the SPB star in the binary system HD 201433 has been spun up by its companion while the inner layers have a much slower and near-rigid rotation. The spin history of KIC 9592855 may be very complex, as it may involve binary evolution with mass transfer as will be discussed in the next section. Possibly, the secondary star in KIC 9592855 had a higher primordial rotation rate, and it has been spun down from the surface inward by its companion and synchronization is achieved before the mass transfer begins. Currently, KIC 9592855 has finished the mass transfer, and thus the secondary has a uniform rotation rate. The measured surface and internal rotation rates can give us a hint about the complicated binary evolutionary history.

In circular and synchronized binaries, the static equilibrium tide mainly affects the high-frequency p-modes, and it can be treated as a perturbation to the second order of rotation (rotational distortion and tidal distortion; Saio 1981). The effect of distortion on g-modes

is small. For binaries with very eccentric orbits, the dynamical tide can induce oscillation modes of mainly $l = 2$ (Welsh et al. 2011; Hambleton et al. 2016; Guo et al. 2017; Pablo et al. 2017). KIC 9592855 apparently falls into the former regime.

3.4. Evolution

To determine the evolutionary state of KIC 9592855, we show the evolution of stellar radius and the asymptotic period spacing of $l = 1$ modes $\Delta\Pi_{l=1}$ in Figure 8. The two sets of tracks can be distinguished by their corresponding colors, where red tracks are for the radius evolution and black tracks are for the period spacing evolution. The solid, dotted, and dashed tracks have associated stellar masses of $1.8M_{\odot}$, $1.7M_{\odot}$, and $1.6 M_{\odot}$, respectively. The observed radii of the primary and secondary star, with $\pm 1\sigma$ credible regions, are indicated by the green and blue shaded horizontal bars, respectively.

We can use a set of vertical lines to infer the age of this system (if they were from single star evolution), taking into account the observed radii of the two stars. The observed radius of the primary star indicates it is close to ZAMS, with an age less than 2×10^8 yrs, and this can be seen from the deep green region where the evolutionary tracks of stellar radii intersect the green bar. However, to explain the observed radius of the secondary star ($R_2 = 1.96R_{\odot}$, the blue bar) using the red evolutionary tracks, we have to adopt a much older age, about 0.7 to 1.15 Gyr (deep blue region). The two stars have an almost identical mass and very different radii, and cannot be explained by a pair of coeval models from single star evolution. With an orbital period of only 1.2 days, and an orbital separation of ~ 7 solar radii, one natural explanation of this contradiction is the binary star evolution with mass transfer. This binary seems to be close to the state of minimum orbital period/separation in the binary evolution when the mass ratio approaches unity. We also repeat the above steps using evolutionary tracks with convective core overshooting ($f_{ov} = 0.02$). Since the main-sequence is extended in this case, the age discrepancy of the two stars actually becomes larger.

Note that we also show the observed period spacing of dipolar modes ($\Delta\Pi_{l=1} = 3.0 \pm 0.2 \times 1000$ seconds, the gray horizontal bar). This gray bar intersects the black tracks (theoretical $\Delta\Pi_{l=1}$ with different masses) at ages of about 7.5×10^8 to 1.4×10^9 yrs, as indicated by the deep gray region. This age range overlaps the previous age range of the secondary star from comparison of stellar radius (deep blue region). It means that evolutionary models with age from 7.5×10^8 to 1.15×10^9 yrs can explain both the observed radius and dipolar mode period spacing. All models with ages less than 2×10^8 yrs in the deep green region have period spacings values (3.4 – 3.6) higher than the observation (3.0 ± 0.2). It is thus

likely that the observed dipolar modes are from the secondary star.

The ages inferred above cannot be adopted as the age of this binary system, but the age discrepancy discussed above reveals convincingly the mass transfer history of this binary. The primary star has typical parameters ($M = 1.72M_{\odot}$, $R = 1.53R_{\odot}$) of a ZAMS star. It is thus likely that it has been rejuvenated in the past, i.e., it is formed by accreting mass from the secondary star. The secondary has a large filling factor ($f_2 = 0.565$), and it may have finished the mass transfer in the not-too-distant past. The system thus becomes detached, and its orbital period will lengthen from the current value. In a sense, KIC 9592855 roughly resembles KIC 8262223 (Guo et al. 2017), another post-mass transfer δ Scuti pulsator with comparable orbital period and separation. The two binaries may have similar evolutionary history.

4. Conclusions and Prospects

We performed photometric and spectroscopic analysis of the post-mass transfer γ Dor/ δ Scuti hybrid pulsating eclipsing binary KIC 9592855. The pulsation spectrum after subtracting the binary light curve shows strong low-frequency g-modes and low-order p-modes. We identify these dominant g-modes as prograde dipole modes. Their near-equally spaced period pattern, which likely arises from the secondary star, reveals a near-uniformly rotating core and envelope. The derived asymptotic period spacing of dipole modes also supports the argument that the observed g-modes are from the secondary. The identical mass but very different radii of the two components strongly suggest that this close binary has a mass-transfer history.

Much work remains to be done to understand this intriguing binary. Albeit challenging, it is worthwhile to model observed p-modes. With a projected equatorial rotational velocity of $\sim 80 \text{ km s}^{-1}$, perturbation to the second order is needed to account for the centrifugal distortion and tidal distortion. It is also highly desirable to perform a detailed binary evolutionary modeling similar to those done by Stępień et al. (2017). If theoretical pulsation frequencies of those observed g-modes or even p-modes can be calculated at different stages of mass transfer, our theory of the close binary evolution can be confronted with observations and thus refined. In this work, only seven radial velocities have been measured. More spectroscopic observations covering the full orbit can improve the fundamental parameters of this binary. The light curve of KIC 9592855 contains relatively wider eclipses, and this makes it a good candidate to implement the eclipse mapping technique.

We thank the *Kepler* team for creating the excellent photometric data used here. We

also express thanks to Jerry Orosz for sharing his ELC code; to Gerald Handler, Alexey Pamyatnykh and Wojciech Dziembowski for providing the NADROT code and helpful discussions; to Jakub Ostrowski and Wojciech Szewczuk for sharing their nice Fortran program connecting MESA and NADROT; to Bill Paxton, Rich Townsend et al. for making MESA and GYRE available; to Hideyuki Saio for helpful discussions on traditional approximation. Z.G. thanks Steven Williams for help in using the ELC code. This work has been supported by the Polish NCN grant 2015/18/A/ST9/00578. This material is based upon work supported by the U.S. National Science Foundation under Grant No. AST-1411654.

Table 1. Atmospheric Parameters

Parameter	Primary ^b	Secondary ^b	Primary ^c	Secondary ^c
T_{eff} (K)	7092 ± 50	7565 ± 57	7074 ± 64	7582 ± 78
$\log g$ (cgs)	4.3^{a}	4.0^{a}	4.3^{a}	4.0^{a}
$v \sin i$ (km s ⁻¹)	64 ± 9	70 ± 10	61 ± 10	75 ± 10
[Fe/H]	-0.06 ± 0.05	0.04 ± 0.05	-0.04 ± 0.04	-0.01 ± 0.03

^a Fixed.

^b Genetic algorithm.

^c Levenberg-Marquardt algorithm.

Table 2. Binary Model Parameters

Parameter	Primary (1)	Secondary (2)	System
Orbital Period (days)			$1.21932483^{\text{a}} \pm 0.00000002$
Time of primary minimum, T_0 (BJD-2400000)			$55691.664073^{\text{a}} \pm 0.00007$
Orbital eccentricity, e			0.0^{a}
Orbital inclination (degree), i			$73.25^{\text{b}} \pm 0.07$
Semi-major axis (R_{\odot}), a			7.24 ± 0.09
Mass ratio $q = M_2/M_1 = K_1/K_2$			$0.99^{\text{b}} \pm 0.03$
Systemic velocity (km s ⁻¹), γ			$8.7^{\text{b}} \pm 0.6$
Mass (M_{\odot})	1.72 ± 0.07	1.71 ± 0.06	
Radius (R_{\odot})	1.53 ± 0.03	1.96 ± 0.03	
Filling factor, f	$0.426^{\text{b}} \pm 0.006$	$0.565^{\text{b}} \pm 0.004$	
Gravity brightening coefficient, β	0.08^{a}	0.08^{a}	
Bolometric albedo, l	$0.32^{\text{b}} \pm 0.04$	$0.34^{\text{b}} \pm 0.05$	
T_{eff} (K)	7300^{a}	$7202^{\text{b}} \pm 70$	
$\log g$ (cgs)	4.30 ± 0.03	4.09 ± 0.03	
Synchronous $v \sin i$ (km s ⁻¹)	61 ± 1	78 ± 1	
Velocity semi-amplitude K (km s ⁻¹)	$143.6^{\text{b}} \pm 2.4$	144.3 ± 4.3	

^aFixed parameters: $P, T_0, e, \beta_1, \beta_2, T_{\text{eff}1}$.

^bFree parameters: $i, f_1, f_2, l_1, l_2, T_{\text{eff}2}, K_1, q, \gamma$.

Table 3. Near Equally-spaced Prograde G-modes

	Period (1000 sec)	Frequency (d^{-1})	Amplitude (10^{-3})	Phase ($\text{rad}/2\pi$)	S/N
f_{24}	30.53811 ± 0.00025	2.82925 ± 0.00002	0.093 ± 0.016	0.480 ± 0.078	10.2
f_9	32.33915 ± 0.00014	2.67168 ± 0.00001	0.192 ± 0.016	0.422 ± 0.039	20.2
f_*	34.04593 ± 0.00088	2.53775 ± 0.00007	0.035 ± 0.017	0.381 ± 0.224	3.6
f_3	35.66299 ± 0.00006	2.42268 ± 0.00001	0.609 ± 0.017	0.190 ± 0.013	60.9
f_6	37.20746 ± 0.00011	2.32212 ± 0.00001	0.353 ± 0.018	0.419 ± 0.023	34.5
f_1	38.69912 ± 0.00003	2.23261 ± 0.00001	1.522 ± 0.018	0.283 ± 0.005	145.7
f_{18}	40.14575 ± 0.00037	2.15216 ± 0.00002	0.125 ± 0.018	0.479 ± 0.068	11.8

^aNote: f_* has S/N < 4 but is included because of its relation to the other g-mode frequencies (see Section 3.3)

Table 4. Other Significant Oscillation Frequencies

	Frequency (d^{-1})	Amplitude (10^{-3})	Phase ($\text{rad}/2\pi$)	S/N	Comment
f_2	24.43343 ± 0.00001	0.290 ± 0.008	0.353 ± 0.012	65.0	
f_4	21.31124 ± 0.00001	0.240 ± 0.008	0.473 ± 0.015	52.2	
f_5	1.95288 ± 0.00001	0.452 ± 0.019	0.502 ± 0.020	40.6	
f_7	9.93593 ± 0.00001	0.308 ± 0.019	0.804 ± 0.029	27.7	
f_8	13.88504 ± 0.00001	0.218 ± 0.015	0.865 ± 0.032	25.2	
f_{10}	24.43296 ± 0.00001	0.085 ± 0.008	0.075 ± 0.042	18.9	
f_{11}	6.56103 ± 0.00001	0.108 ± 0.011	0.201 ± 0.046	17.4	
f_{12}	4.92074 ± 0.00002	0.096 ± 0.011	0.283 ± 0.051	15.5	$f_{11} - 2f_{orb}$
f_{13}	1.28384 ± 0.00002	0.204 ± 0.023	0.708 ± 0.052	15.5	
f_{14}	19.18962 ± 0.00002	0.087 ± 0.010	0.590 ± 0.053	15.0	
f_{15}	3.93411 ± 0.00002	0.102 ± 0.012	0.894 ± 0.056	14.1	
f_{16}	18.16594 ± 0.00002	0.103 ± 0.013	0.887 ± 0.057	13.9	
f_{17}	0.74094 ± 0.00002	0.193 ± 0.026	0.811 ± 0.064	12.5	
f_{19}	10.58986 ± 0.00002	0.128 ± 0.020	0.958 ± 0.071	11.2	
f_{20}	24.43401 ± 0.00002	0.049 ± 0.008	0.799 ± 0.073	10.9	
f_{21}	20.82988 ± 0.00002	0.052 ± 0.008	0.367 ± 0.073	10.9	$f_{14} + 2f_{orb}$
f_{22}	18.81166 ± 0.00002	0.068 ± 0.011	0.111 ± 0.074	10.7	
f_{23}	8.20127 ± 0.00002	0.091 ± 0.015	0.506 ± 0.076	10.6	$f_{11} + 2f_{orb}$
f_{25}	23.37736 ± 0.00003	0.040 ± 0.007	0.921 ± 0.086	9.3	
f_{26}	16.79271 ± 0.00003	0.074 ± 0.014	0.748 ± 0.090	8.8	
f_{27}	0.78244 ± 0.00003	0.125 ± 0.026	0.443 ± 0.097	8.2	$f_3 - 2f_{orb}$
f_{28}	1.25028 ± 0.00003	0.109 ± 0.023	0.109 ± 0.097	8.2	
f_{29}	10.75605 ± 0.00003	0.088 ± 0.020	0.139 ± 0.103	7.7	$f_7 + f_{orb}$
f_{30}	11.65240 ± 0.00003	0.084 ± 0.019	0.015 ± 0.106	7.5	$f_1 - f_8$
f_{31}	11.18603 ± 0.00003	0.080 ± 0.019	0.675 ± 0.114	7.0	
f_{32}	0.01079 ± 0.00003	0.129 ± 0.032	0.368 ± 0.117	6.8	
f_{33}	8.76189 ± 0.00003	0.065 ± 0.016	0.780 ± 0.117	6.8	
f_{34}	3.28051 ± 0.00003	0.056 ± 0.014	0.876 ± 0.118	6.8	$f_{12} - 2f_{orb}$
f_{35}	0.69291 ± 0.00004	0.103 ± 0.027	0.930 ± 0.121	6.6	
f_{36}	14.76231 ± 0.00004	0.050 ± 0.013	0.724 ± 0.121	6.6	
f_{37}	21.73707 ± 0.00004	0.029 ± 0.008	0.975 ± 0.125	6.4	$f_{25} - 2f_{orb}$
f_{38}	0.59236 ± 0.00004	0.102 ± 0.028	0.978 ± 0.126	6.3	$f_1 - 2f_{orb}$
f_{39}	7.70329 ± 0.00004	0.048 ± 0.013	0.117 ± 0.127	6.3	$f_7 - f_1$

Table 4—Continued

	Frequency (d^{-1})	Amplitude (10^{-3})	Phase ($\text{rad}/2\pi$)	S/N	Comment
f_{40}	13.88551 ± 0.00004	0.054 ± 0.015	0.605 ± 0.128	6.2	
f_{41}	20.49110 ± 0.00004	0.030 ± 0.008	0.515 ± 0.129	6.2	$f_4 - f_{orb}$
f_{42}	21.32186 ± 0.00004	0.028 ± 0.008	0.626 ± 0.131	6.1	
f_{43}	13.10256 ± 0.00004	0.059 ± 0.017	0.970 ± 0.132	6.0	
f_{44}	7.26424 ± 0.00004	0.042 ± 0.012	0.669 ± 0.134	6.0	$f_7 - f_9$
f_{45}	10.96873 ± 0.00004	0.066 ± 0.020	0.479 ± 0.137	5.8	
f_{46}	9.35431 ± 0.00004	0.061 ± 0.018	0.498 ± 0.137	5.8	
f_{47}	1.72521 ± 0.00004	0.067 ± 0.020	0.224 ± 0.139	5.7	
f_{48}	1.60257 ± 0.00004	0.068 ± 0.021	0.424 ± 0.143	5.6	$f_3 - f_{orb}$
f_{49}	1.41253 ± 0.00004	0.070 ± 0.022	0.512 ± 0.146	5.5	$f_1 - f_{orb}$
f_{50}	0.00558 ± 0.00004	0.102 ± 0.032	0.396 ± 0.147	5.4	
f_{51}	3.07663 ± 0.00004	0.046 ± 0.015	0.216 ± 0.151	5.3	
f_{52}	21.31071 ± 0.00004	0.024 ± 0.008	0.189 ± 0.153	5.2	$f_{42} - 2f_{50}$
f_{53}	11.57612 ± 0.00005	0.058 ± 0.019	0.101 ± 0.155	5.2	
f_{54}	2.49515 ± 0.00005	0.051 ± 0.017	0.869 ± 0.155	5.1	
f_{55}	12.26919 ± 0.00005	0.055 ± 0.018	0.558 ± 0.156	5.1	
f_{56}	1.24949 ± 0.00005	0.068 ± 0.023	0.420 ± 0.157	5.1	
f_{57}	2.38117 ± 0.00005	0.051 ± 0.017	0.225 ± 0.157	5.1	$f_{17} + 2f_{orb}$
f_{58}	21.05471 ± 0.00005	0.024 ± 0.008	0.431 ± 0.159	5.0	
f_{59}	9.96933 ± 0.00005	0.056 ± 0.019	0.389 ± 0.159	5.0	
f_{60}	0.00915 ± 0.00005	0.088 ± 0.032	0.485 ± 0.171	4.7	
f_{61}	0.01408 ± 0.00005	0.086 ± 0.032	0.643 ± 0.174	4.6	
f_{62}	0.00719 ± 0.00005	0.085 ± 0.032	0.115 ± 0.177	4.5	
f_{63}	7.51321 ± 0.00005	0.033 ± 0.013	0.543 ± 0.177	4.5	$f_7 - f_3$
f_{64}	3.05276 ± 0.00005	0.039 ± 0.015	0.643 ± 0.178	4.5	$f_1 + f_{orb}$
f_{65}	2.18949 ± 0.00005	0.047 ± 0.018	0.709 ± 0.179	4.5	
f_{66}	20.00926 ± 0.00005	0.023 ± 0.009	0.403 ± 0.180	4.4	
f_{67}	3.87292 ± 0.00005	0.032 ± 0.012	0.336 ± 0.182	4.4	$f_1 + 2f_{orb}$
f_{68}	19.67112 ± 0.00005	0.023 ± 0.009	0.386 ± 0.183	4.4	
f_{69}	3.24279 ± 0.00005	0.036 ± 0.014	0.543 ± 0.184	4.3	$f_3 + f_{orb}$
f_{70}	0.04100 ± 0.00005	0.080 ± 0.032	0.630 ± 0.186	4.3	
f_{71}	3.50826 ± 0.00006	0.033 ± 0.013	0.505 ± 0.189	4.2	
f_{72}	5.14855 ± 0.00006	0.025 ± 0.010	0.339 ± 0.189	4.2	

Table 4—Continued

	Frequency (d^{-1})	Amplitude (10^{-3})	Phase ($\text{rad}/2\pi$)	S/N	Comment
f_{73}	10.14854 ± 0.00006	0.047 ± 0.019	0.853 ± 0.189	4.2	$f_{45} - f_{orb}$
f_{74}	14.61031 ± 0.00006	0.032 ± 0.013	0.264 ± 0.189	4.2	
f_{75}	9.84149 ± 0.00006	0.046 ± 0.019	0.553 ± 0.193	4.1	
f_{76}	19.68325 ± 0.00006	0.022 ± 0.009	0.630 ± 0.195	4.1	
f_{77}	9.15351 ± 0.00006	0.041 ± 0.017	0.098 ± 0.196	4.1	

REFERENCES

- Armstrong, D. J., Gomez Maqueo Chew, Y., Faedi, F., & Pollacco, D. 2014, MNRAS, 437, 3473
- Bagnuolo, W. G., Jr., & Gies, D. R. 1991, ApJ, 376, 266
- Bedding, T. R., Murphy, S. J., Colman, I. L., & Kurtz, D. W. 2015, European Physical Journal Web of Conferences, 101, 01005
- Bíró, I. B., & Nuspl, J. 2011, MNRAS, 416, 1601
- Borucki, W. J., Koch, D., Basri, G., et al. 2010, Science, 327, 977
- Briquet, M., Morel, T., Thoul, A., et al. 2007, MNRAS, 381, 1482
- Brown, T. M., Latham, D. W., Everett, M. E., & Esquerdo, G. A. 2011, AJ, 142, 112
- Çakırh, Ö., Ibanoglu, C., Sipahi, E., & Akan, M. C. 2017, New A, 52, 96
- Charbonneau, P. 1995, ApJS, 101, 309
- Chen, X., Maxted, P. F. L., Li, J., & Han, Z. 2017, MNRAS, in press
- Conroy, K. E., Prša, A., Stassun, K. G., et al. 2014, AJ, 147, 45
- Czekala, I., Mandel, K. S., Andrews, S. M., et al. 2017, arXiv:1702.05652
- Debosscher, J., Blomme, J., Aerts, C., & De Ridder, J. 2011, A&A, 529, A89
- Dotter, A., Chaboyer, B., Jevremović, D., et al. 2008, ApJS, 178, 89
- Dupret, M.-A., Thoul, A., Scuflaire, R., et al. 2004, A&A, 415, 251
- Dupret, M.-A., Grigahcène, A., Garrido, R., Gabriel, M., & Scuflaire, R. 2005, A&A, 435, 927
- Dziembowski, W. A. 1971, Acta Astron., 21, 289
- Dziembowski, W. 1977, Acta Astron., 27, 95
- Gautschy, A., & Saio, H. 2017, arXiv:1704.00124
- Gies, D. R., Williams, S. J., Matson, R. A., et al. 2012, AJ, 143, 137
- Gies, D. R., Matson, R. A., Guo, Z., et al. 2015, AJ, 150, 178

- Gizon, L., & Solanki, S. K. 2003, *ApJ*, 589, 1009
- Goldreich, P., & Nicholson, P. D. 1989, *ApJ*, 342, 1079
- Grevesse, N., & Sauval, A. J. 1998, *Space Sci. Rev.*, 85, 161
- Guo, Z., Gies, D. R., Matson, R. A., & García Hernández, A. 2016, *ApJ*, 826, 69
- Guo, Z., Gies, D. R., & Fuller, J. 2017, *ApJ*, 834, 59
- Guo, Z., Gies, D. R., Matson, R. A., et al. 2017, *ApJ*, 837, 114
- Guzik, J. A., Kaye, A. B., Bradley, P. A., Cox, A. N., & Neuforge, C. 2000, *ApJ*, 542, L57
- Hadrava, P. 1995, *A&AS*, 114, 393
- Hambleton, K., Kurtz, D. W., Prša, A., et al. 2016, *MNRAS*, 463, 1199
- Hauschildt, P. H., Allard, F., & Baron, E. 1999, *ApJ*, 512, 377
- Huber, D., Silva Aguirre, V., Matthews, J. M., et al. 2014, *ApJS*, 211, 2
- Iglesias, C. A., & Rogers, F. J. 1996, *ApJ*, 464, 943
- Ilijic, S., Hensberge, H., Pavlovski, K., & Freyhammer, L. M. 2004, (ASP Conf. Vol. 318), ed. R. W. Hilditch, H. Hensberge, & K. Pavlovski, (San Francisco: ASP), 111
- Kallinger, T., Reegen, P., & Weiss, W. W. 2008, *A&A*, 481, 571
- Kallinger, T., Weiss, W. W., Beck, P. G., et al. 2017, *arXiv:1704.01151*
- Karczmarek, P., Wiktorowicz, G., Iłkiewicz, K., et al. 2017, *MNRAS*, 466, 2842
- Kirk, B., Conroy, K., Prša, A., et al. 2016, *AJ*, 151, 68
- Kurtz, D. W., Saio, H., Takata, M., et al. 2015, *European Physical Journal Web of Conferences*, 101, 01007
- Lenz, P., & Breger, M. 2005, *Communications in Asteroseismology*, 146, 53
- Matson, R. A., Gies, D. R., Guo, Z., & Orosz, J. A. 2016, *AJ*, 151, 139
- Miglio, A., Montalbán, J., Noels, A., & Eggenberger, P. 2008, *MNRAS*, 386, 1487
- Mkrtichian, D. E., Kusakin, A. V., Gamarova, A. Y., et al. 2002, in *Observational Aspects of Pulsating B- and A Stars*, (ASP Conf. Vol. 256), ed. C. Sterken & D. W. Kurtz (San Francisco: ASP), 259

- Mkrtichian, D. E., Nazarenko, V., Gamarova, A. Y., et al. 2003, in *Interplay of Periodic, Cyclic and Stochastic Variability in Selected Areas of the H-R Diagram*, (ASP Conf. Vol. 292), ed. C. Sterken (San Francisco: ASP), 113
- Murphy, S. J., Bedding, T. R., Shibahashi, H., Kurtz, D. W., & Kjeldsen, H. 2014, *MNRAS*, 441, 2515
- Murphy, S. J., Fossati, L., Bedding, T. R., et al. 2016, *MNRAS*, 459, 1201
- Orosz, J. A., & Hauschildt, P. H. 2000, *A&A*, 364, 265
- Ouazzani, R.-M., Salmon, S. J. A. J., Antoci, V., et al. 2017, *MNRAS*, 465, 2294
- Pablo, H., Richardson, N. D., Fuller, J., et al. 2017, *MNRAS*, 467, 2494
- Pamyatnykh, A. A. 1999, *Acta Astron.*, 49, 119
- Pamyatnykh, A. A., Handler, G., & Dziembowski, W. A. 2004, *MNRAS*, 350, 1022
- Pápics, P. I., Tkachenko, A., Aerts, C., et al. 2015, *ApJ*, 803, L25
- Pápics, P. I., Tkachenko, A., Van Reeth, T., et al. 2017, *A&A*, 598, A74
- Paxton, B., Bildsten, L., Dotter, A., et al. 2011, *ApJS*, 192, 3
- Paxton, B., Cantiello, M., Arras, P., et al. 2013, *ApJS*, 208, 4
- Paxton, B., Marchant, P., Schwab, J., et al. 2015, *ApJS*, 220, 15
- Pigulski, A., Pojmański, G., Pilecki, B., & Szczygieł, D. M. 2009, *Acta Astron.*, 59, 33
- Pinsonneault, M. H., An, D., Molenda-Żakowicz, J., et al. 2012, *ApJS*, 199, 3
- Prša, A., Batalha, N., Slawson, R. W., et al. 2011, *AJ*, 141, 83
- Prša, A., Degroote, P., Conroy, K., et al. 2013, *EAS Publications Series*, 64, 259
- Reed, M. D., Brondel, B. J., & Kawaler, S. D. 2005, *ApJ*, 634, 602
- Rodríguez-Merino, L. H., Chavez, M., Bertone, E., & Buzzoni, A. 2005, *ApJ*, 626, 411
- Rogers, T. M., Lin, D. N. C., McElwaine, J. N., & Lau, H. H. B. 2013, *ApJ*, 772, 21
- Rogers, T. M. 2015, *ApJ*, 815, L30
- Schmid, V. S., Tkachenko, A., Aerts, C., et al. 2015, *A&A*, 584, A35

- Schmid, V. S., & Aerts, C. 2016, *A&A*, 592, A116
- Shibahashi, H., & Kurtz, D. W. 2012, *MNRAS*, 422, 738
- Slawson, R. W., Prša, A., Welsh, W. F., et al. 2011, *AJ*, 142, 160
- Stellingwerf, R. F. 1978, *AJ*, 83, 1184
- Stępień, K., Pamyatnykh, A. A., & Rozyczka, M. 2017, *A&A*, 597, A87
- Tassoul, M. 1980, *ApJS*, 43, 469
- Townsend, R. H. D. 2005, *MNRAS*, 360, 465
- Townsend, R. H. D., & Teitler, S. A. 2013, *MNRAS*, 435, 3406
- Triana, S. A., Moravveji, E., Pápics, P. I., et al. 2015, *ApJ*, 810, 16
- Unno, W., Osaki, Y., Ando, H., Saio, H., & Shibahashi, H. 1989, *Nonradial oscillations of stars*, Tokyo: University of Tokyo Press, 1989, 2nd ed.,
- Van Reeth, T., Tkachenko, A., Aerts, C., et al. 2015, *A&A*, 574, A17
- Van Reeth, T., Tkachenko, A., Aerts, C., et al. 2015, *ApJS*, 218, 27
- Van Reeth, T., Tkachenko, A., & Aerts, C. 2016, *A&A*, 593, A120
- Vos, J., Østensen, R. H., Marchant, P., & Van Winckel, H. 2015, *A&A*, 579, A49
- Walker, G., Matthews, J., Kuschnig, R., et al. 2003, *PASP*, 115, 1023
- Welsh, W. F., Orosz, J. A., Aerts, C., et al. 2011, *ApJS*, 197, 4
- Xiong, D. R., Cheng, Q. L., & Deng, L. 1997, *ApJS*, 108, 529
- Xiong, D. R., Deng, L., & Zhang, C. 2015, *MNRAS*, 451, 3354
- Xiong, D. R., Deng, L., Zhang, C., & Wang, K. 2016, *MNRAS*, 457, 3163
- Zahn, J.-P. 1975, *A&A*, 41, 329
- Zahn, J.-P. 2008, *EAS Publications Series*, 29, 67
- Zwintz, K., Moravveji, E., Papics, P. I., et al. 2017, *arXiv:1703.06456*

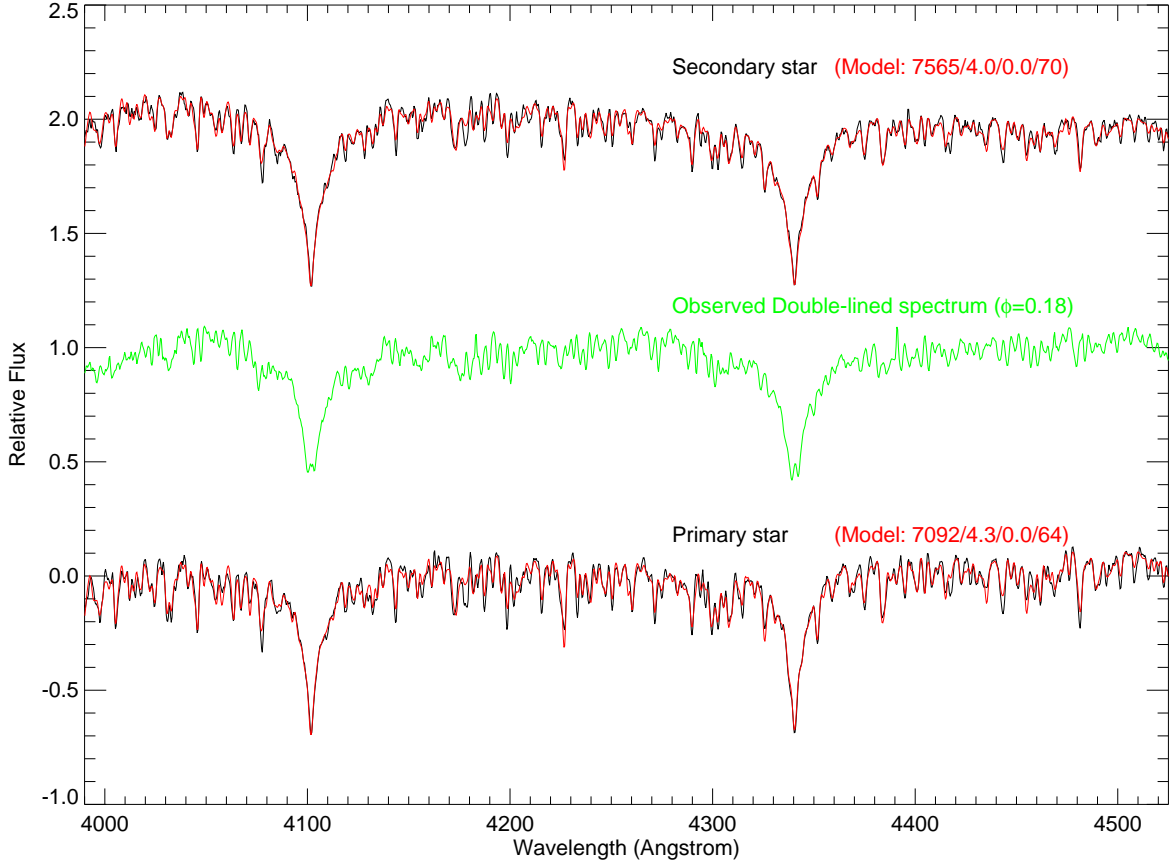


Fig. 1.— The observed composite spectrum at orbital phase $\phi = 0.18$ is shown as the green line. The tomographic reconstructed individual spectrum of the primary and secondary star are indicated by the black lines (shifted downward and upward respectively for clarity), with the best-fitting model from UVBLUE over-plotted in red. The atmospheric parameters of the models are shown in the parentheses, in the order of $T_{\text{eff}}(\text{K}) / \log g(\text{cgs}) / [\text{Fe}/\text{H}](\text{dex}) / v \sin i(\text{km s}^{-1})$.

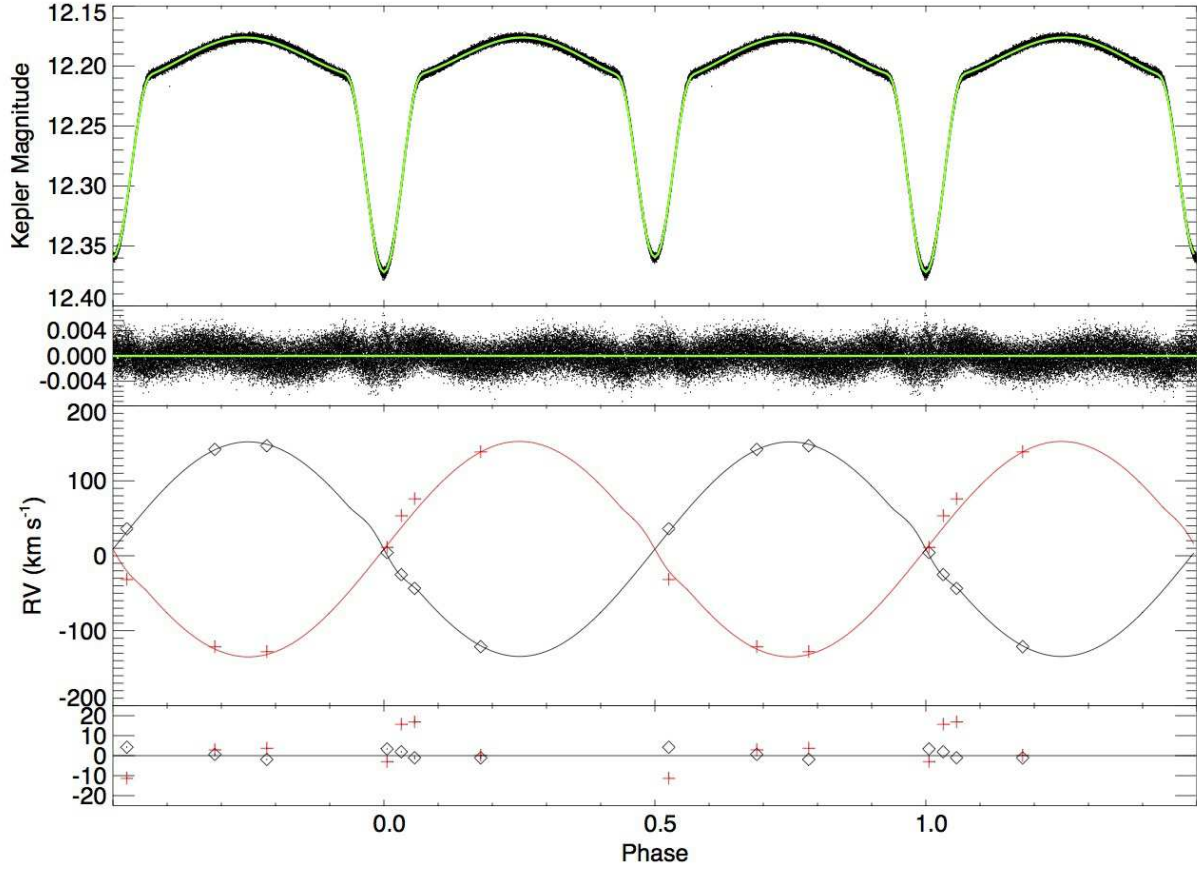


Fig. 2.— The upper and lower panels show the *Kepler* light curve (black dots) and radial velocities derived by Matson et al. (2017 in prep.), respectively. The measured RVs of the primary and the secondary star are indicated by the diamonds and crosses, respectively. The best-fitting binary models from ELC code are over-plotted, with the green line indicating the light curve model and black/red lines for the radial velocity models.

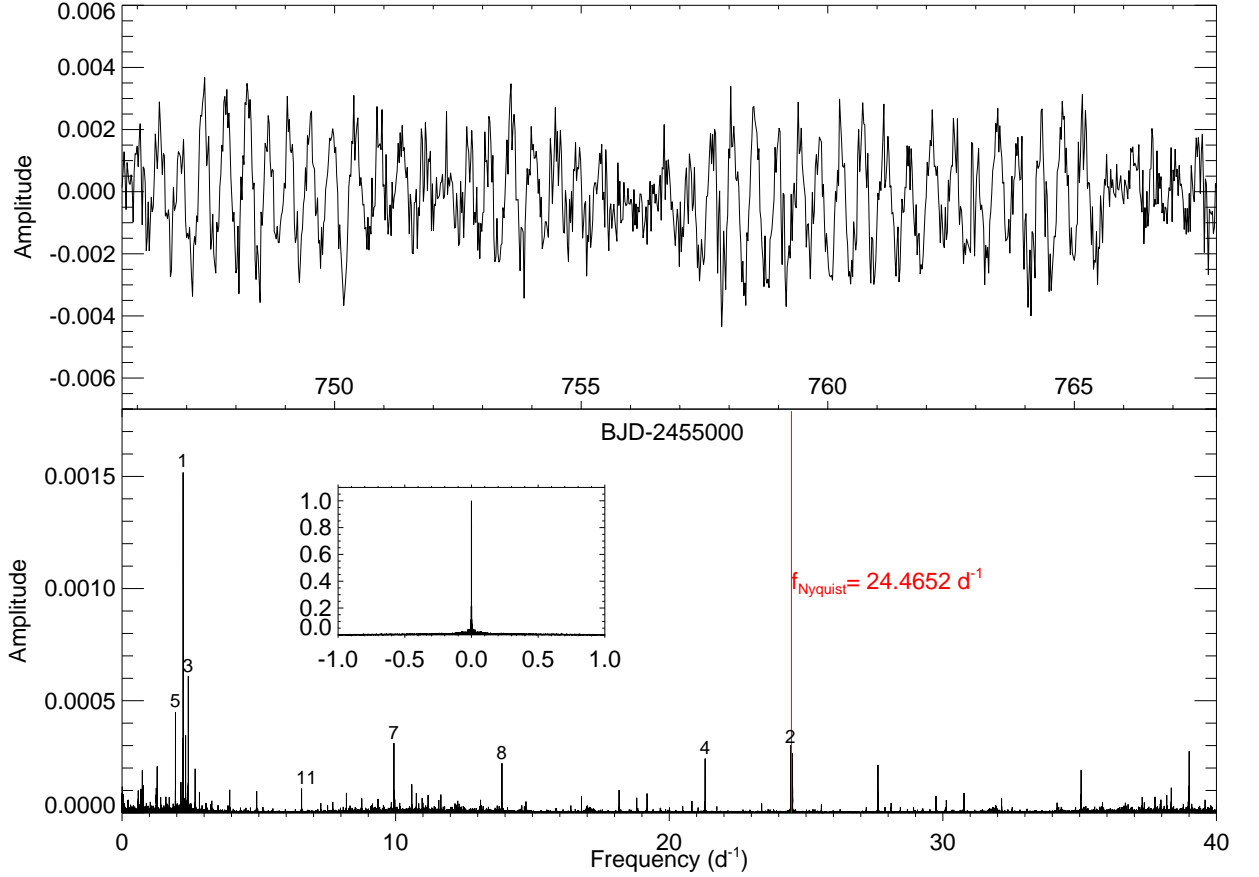


Fig. 3.— Time series of *Kepler* photometric data of oscillations with the binary light curve subtracted in the time domain (upper) and frequency domain (lower). Several of the strongest pulsation peaks have been labeled by their frequency numbers (Table 3 and 4). The inset in the lower panel shows the spectral window. The Fourier spectrum in the super-Nyquist region is also shown, with the red vertical line indicating the Nyquist frequency $f_{\text{Nyquist}} = 24.4652 \text{ d}^{-1}$ of *Kepler* long cadence data. All pulsations in the super-Nyquist region have lower amplitudes compared to their mirror reflections around the f_{Nyquist} , indicating they are not real pulsation peaks, but are aliases.

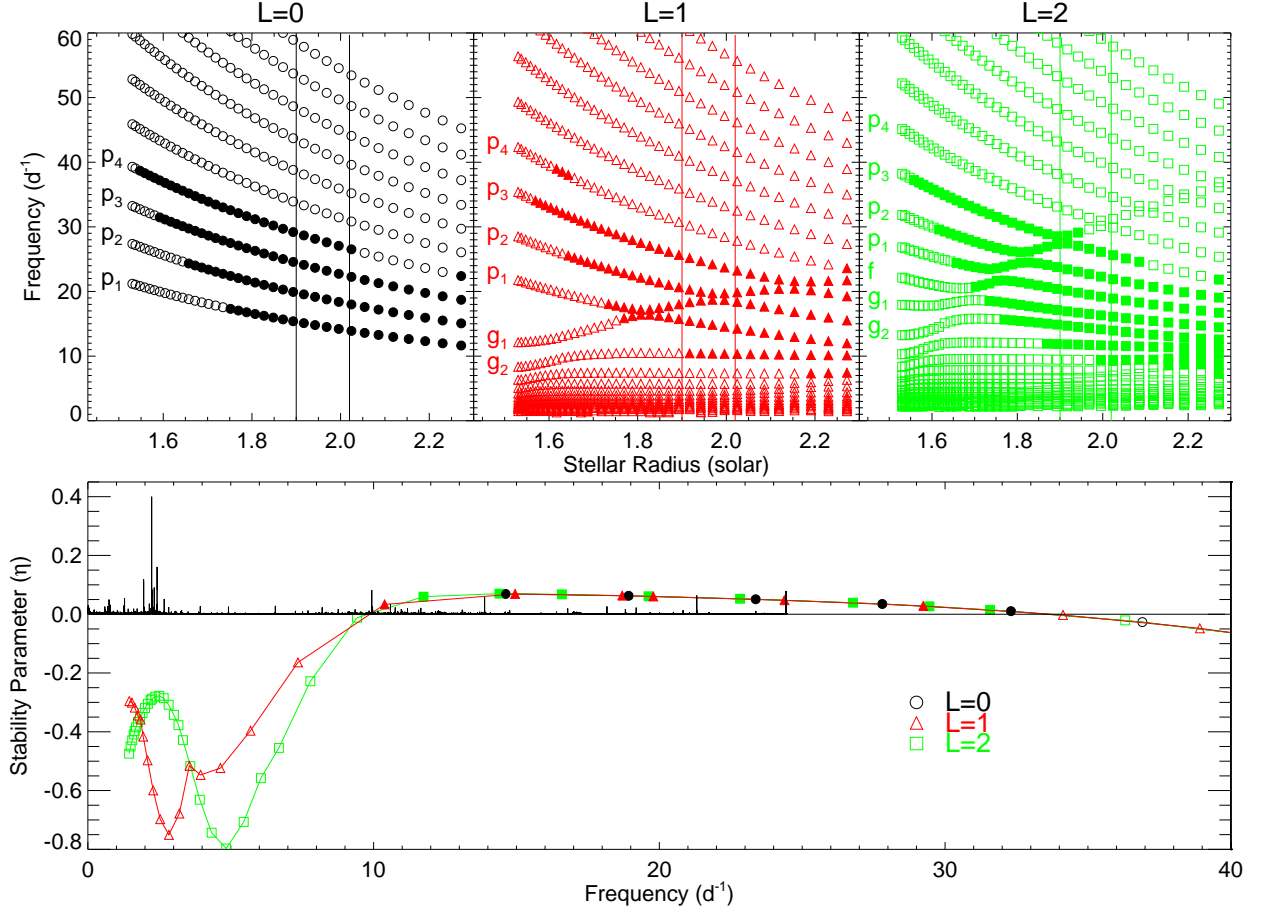


Fig. 4.— **Upper panel:** The evolution of theoretical pulsation frequencies of $l = 0, 1, 2$ modes (black circles, red triangles, and green squares, respectively) of a stellar model with $M = 1.70M_{\odot}$. The evolution is shown from ZAMS ($R = 1.5R_{\odot}$) to near TAMS ($R = 2.3R_{\odot}$). The observed radius of the secondary star ($R = 1.96 \pm 0.06R_{\odot}$) is enclosed by the two vertical lines in each sub-panel. The open and filled symbols represent the stable and unstable modes, respectively. **Lower panel:** The stability parameter η of the pulsation modes of the best-matching model with a radius of $R = 1.96R_{\odot}$. For clarity, the observed Fourier spectrum is over-plotted and scaled to have a maximum amplitude of 0.4.

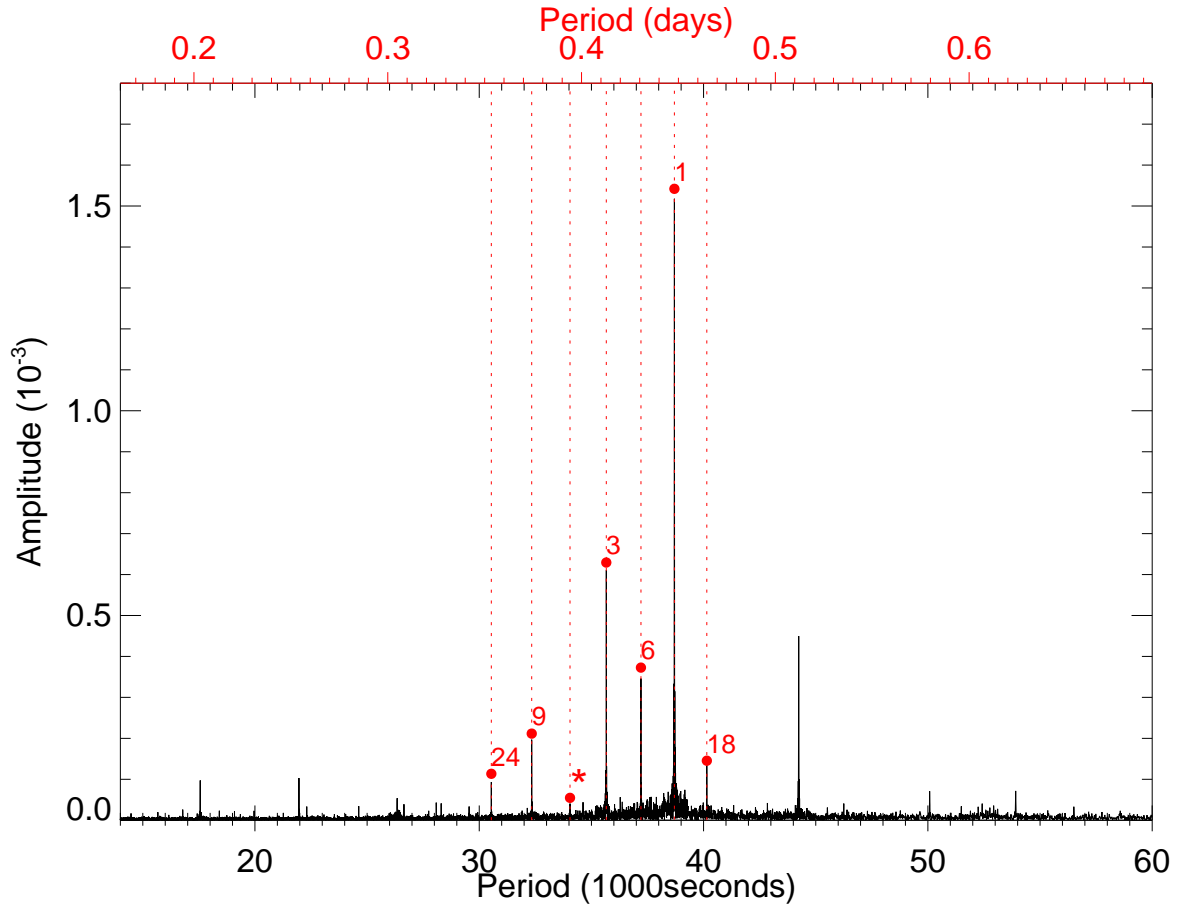


Fig. 5.— The Fourier amplitude spectrum of the g-mode region. The red dotted lines mark the identified series of dipole modes.

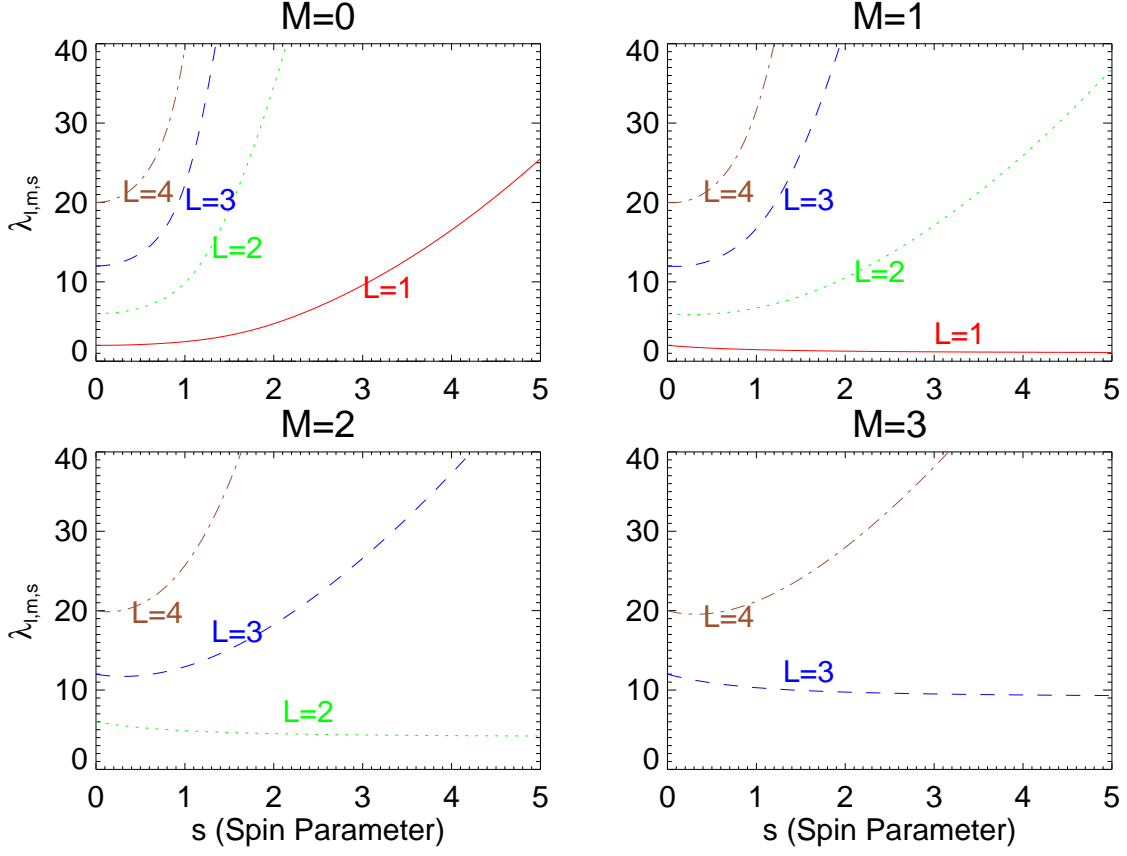


Fig. 6.— The eigenvalues of the Laplace tidal equations $\lambda_{l,m,s}$

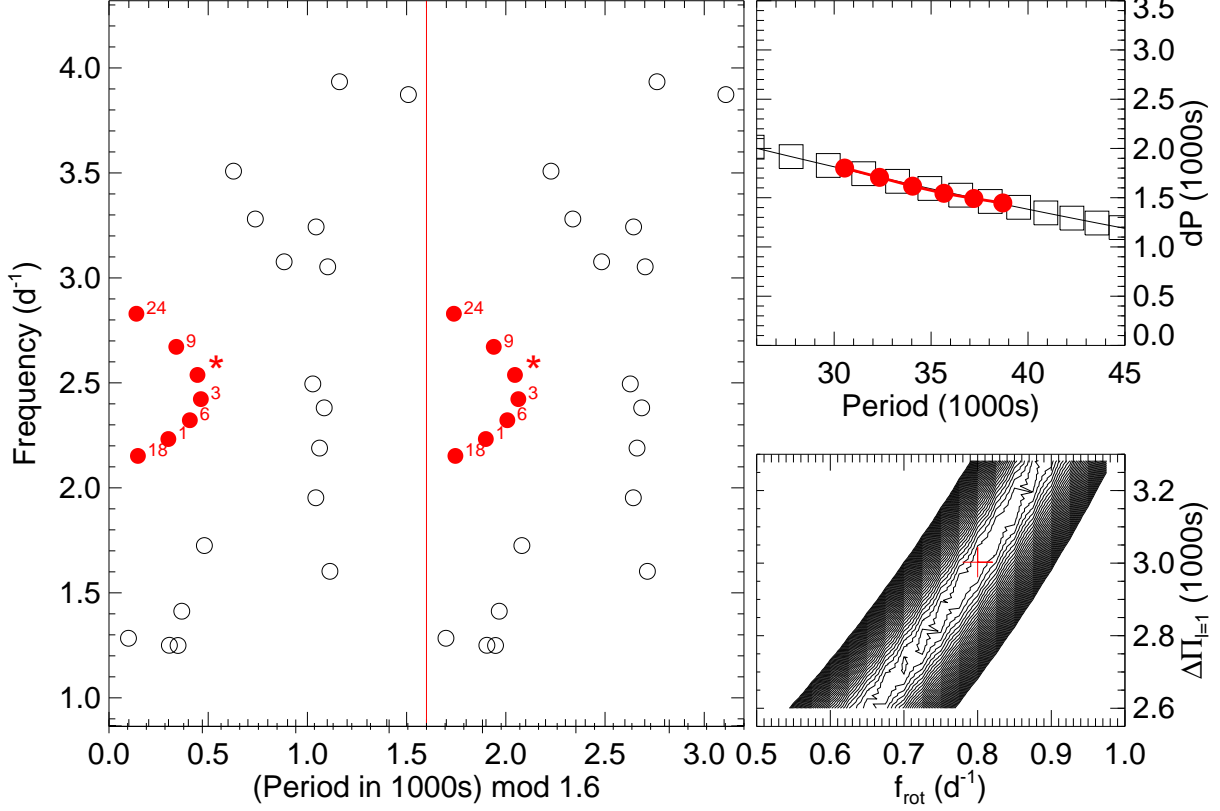


Fig. 7.— **Left**: The period echelle diagram of observed pulsation modes, plotted twice for clarity. Red symbols represent the identified prograde dipole g-modes around $\sim 2.2 \text{ day}^{-1}$. Their corresponding frequency numbers in Table 3 are labeled. **Upper right**: The observed period spacing vs. period ($dP - P$) diagram for the identified $l = 1, m = 1$ g-modes (red symbols). The best-fitting model from the asymptotic period relations in the traditional approximation (eq. 3) is shown as open squares (see text). **Lower right**: The χ^2 contour from fitting the observed $dP - P$. The innermost contour indicates the 1σ credible region. The best solution ($\Delta\Pi_{l=1} = 3000 \text{ sec}$, $f_{\text{rot}} = 0.8 \text{ d}^{-1}$) is marked by the red cross.

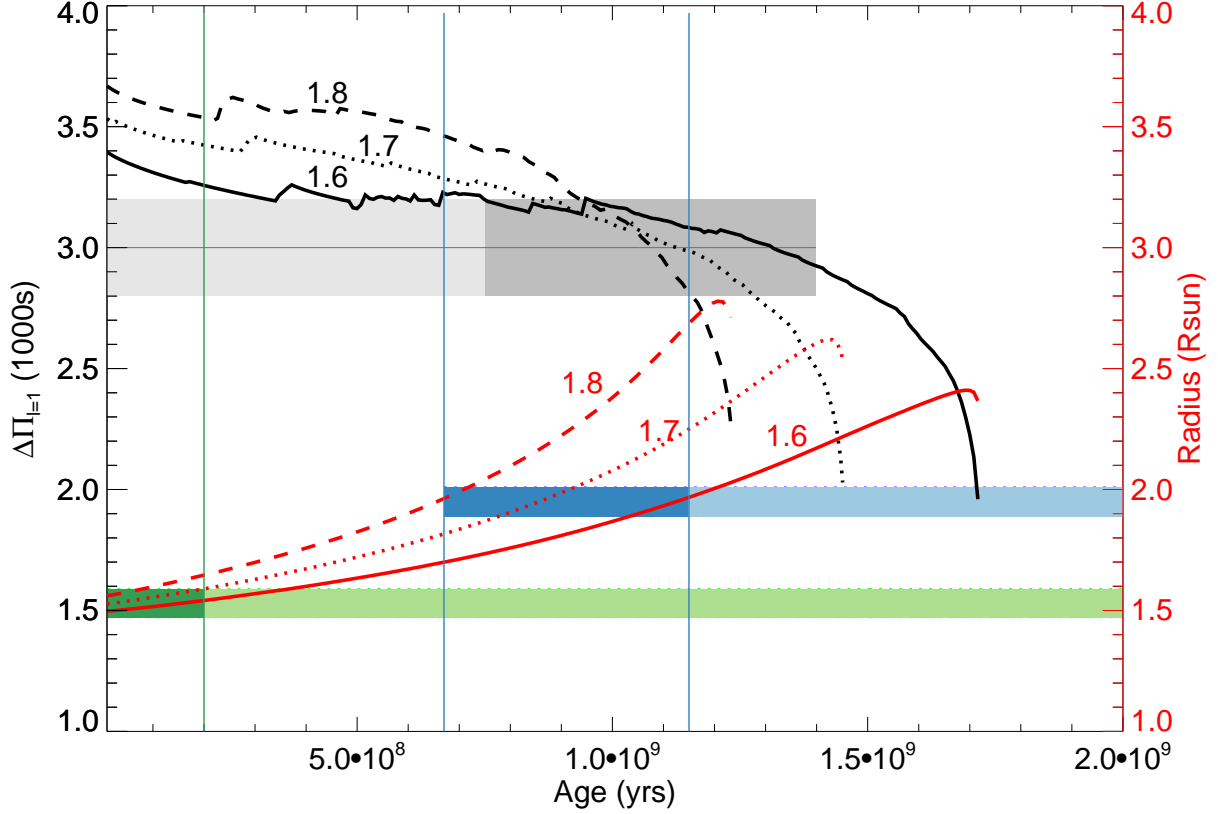


Fig. 8.— Evolutionary tracks of the stellar radius (red lines) and the asymptotic dipolar mode period spacing $\Delta\Pi_{l=1}$ (black lines). Tracks with masses of $1.6M_{\odot}$, $1.7M_{\odot}$ and $1.8M_{\odot}$ are shown as solid, dotted, and dashed lines, respectively. The green and blue horizontal bars indicate the observed stellar radius of the primary and secondary star, respectively. The observed period spacing of dipolar modes is shown as the gray shaded bar. The deep green, deep blue, and deep gray shaded regions represent the positions on the tracks where models match the observations. The deep gray and deep blue regions overlap in age, suggesting that the observed $l = 1, m = 1$ modes originate from the secondary star. Coeval models cannot simultaneously explain the observed radius of the primary and the secondary, and this can be seen from the non-overlapping of the deep green and deep blue regions in age.